Theoretical Assessment of Electrical Steel Magnetic Components During PWM-Type Conversion: A Comparison Between Two Hysteresis Models.

Shengze Gao, Benjamin Ducharne, Yanhui Gao, Xiaojun Zhao

Theoretical Assessment of Electrical Steel Magnetic Components During PWM-Type Conversion: A Comparison Between Two Hysteresis Models

Shengze Gao[1,2], Benjamin Ducharne[3,4], Yanhui Gao[2], and Xiaojun Zhao[1]

[1] Department of Electrical Engineering, North China Electric Power University, Baoding, 071003, China
[2] Faculty of Science and Technology, Oita University, Oita, 870-1192, Japan
[3] ELyTMaX IRL3757, CNRS, Univ. Lyon, INSA Lyon, Centrale Lyon, Universite Claude Bernard Lyon 1, Tohoku University, Sendai, Japan
[4] Univ Lyon, INSA-Lyon, LGEF EA682, F69621, France

Abstract

Accurate simulations of frequency-dependent hysteresis cycles and the associated power losses within electrical steel magnetic components during PWM-type conversion are essential, as they provide crucial insights into converter efficiency and performance. To this end, this study aims to compare two hysteresis models; one combines the Maxwell diffusion equation and a fractional differential equation material law, and the other is based on Bertotti's loss separation theory, extended to include the skin effect. Criteria such as accuracy, simulation time, and number of parameters, among others, aid in determining the most suitable simulation approach. This paper gives precise definitions of the simulation methods, presents comparative results, and draws specific conclusions pertinent to the industrial context.

Keywords

Electrical steel, magnetic hysteresis, magnetic losses, PWM.

I - Introduction

Magnetic components, including inductors and transformers, play crucial functions within PWM-type converters by efficiently storing and transferring energy. Inductors are used to smooth out the current flow. They store energy during the switch's active period and discharge it during the inactive phase, ensuring a continuous output current. Similarly, transformers modulate input voltage to the desired level. They facilitate energy transfer from input to output by inducing secondary winding voltage based on primary winding energy exchange [1, 2]. Magnetic cores necessitate meticulous selection for optimal performance. Core materials such as ferrite, iron powder, and various laminated steel types are commonly utilized, with the choice contingent upon operational frequency, power rating, and cost considerations [3].

Electrical steel, also known as silicon steel or transformer steel, constitutes a specialized steel family engineered for superior soft magnetic properties [4]. Its application in PWM-type converters is recommended due to its minimal core losses, high magnetic permeability, elevated saturation flux density, low magnetostriction, and robust temperature resilience. Accurate simulation of magnetic core losses within PWM converters is imperative. It yields critical insights into converter efficiency and performance, allowing engineers to refine designs for reduced energy dissipation and enhanced reliability [5]. Through precise core loss modeling, designers can forecast temperature elevation, pinpoint potential hotspots, and ensure magnetic components operate within designated safety parameters, thereby fostering the development of more efficient and dependable power conversion systems.

To this end, this study compares two hysteresis models. The first model combines the Maxwell diffusion equation and a fractional differential equation material law. The second model is based on the extension of Bertotti's loss separation theory to include the skin effect.

During PWM-type conversion, ferromagnetic components are commonly stimulated by two types of magnetic field contributions: a high-amplitude, low-frequency fundamental waveform (which induces a major hysteresis cycle) and low-amplitude, high-frequency harmonics (which induce minor hysteresis loops). In this comparative study, both nature of waveforms have guided the selection of the testing conditions. Additionally, actual PWM-type waveforms were tested for validation.

Criteria, including accuracy, simulation time, number of parameters, etc., were used to identify the optimal simulation approach.

This paper defines successively the simulation methods, offers comparative results, and deduces specific conclusions relevant to industrial applications.

II – Magnetic hysteresis models

Hysteresis models are crucial in understanding and predicting the behavior of magnetic materials under PWM-specific working conditions [6]. These models describe the lag between the applied magnetic field measured on the tested specimen's surface (H_{surf}) and the resulting magnetic flux density averaged through its cross-section (B_a). Accurate hysteresis models predict energy dissipation and help quantify the magnetic losses, enabling the design of materials and PWM-type converters with maximized energy efficiencies.

A. 1st Hysteresis Model: Combining the Maxwell Diffusion Equation and a Fractional Differential Equation Material Law.

The first hysteresis model tested in this study was built upon a method initially introduced in [7]. This method involves simultaneously solving the Maxwell diffusion equation (Eq. (1), where σ is the electrical conductivity) and a hysteretic dynamic material law (Eq. (2)). The specific dimensions of the electrical specimens tested in this work (thickness ζ << width, length) allow us to solve the diffusion equation in one dimension (1D) using finite differences while maintaining accurate results. For the material law, the most accessible approach would be to use a quasi-static hysteresis model $H_{stat}(x, B(x,t))$, where $B(x,t)$ would be the local flux density, $H(x,t)$ the local excitation field and H_{stat} an equivalent static excitation field contribution (Preisach model [8], Jiles-Atherton model [9] or equivalent [10]). Still, it would inevitably lead to inaccuracies as it does not account for the excess loss contribution. In [7], a first-order differential equation akin to a viscous behavior was proposed for better accuracy:

$$\sigma \frac{\partial B(x,t)}{\partial t} = \frac{\partial^2 H(x,t)}{\partial x^2} \tag{1}$$

$$\rho \frac{\mathrm{d}B(x,t)}{\mathrm{d}t} = H(x,t) - H_{stat}(B(x,t)) \tag{2}$$

Solving simultaneously Eq. (1) and Eq. (2) makes $B(x,t)$ frequency-dependent, with ρ becoming the unique parameter controlling this effect. This approach is straightforward but restricts a good level of accuracy to a limited frequency bandwidth. The dynamic material law is mainly associated with the kinetic nature of magnetic domains during the magnetization cycle. The magnetic domain motions are not fully viscous (unlike Eq. (2)) but also slightly elastic due to the complex interplay of forces within the material [11]. This elasticity arises from the intrinsic material properties and the interactions between domains, which resist complete and permanent deformation. Consequently, material laws combining a viscous dissipation and an elastic restoration provide a more accurate description of the energy dynamics within magnetic materials. To account for this viscoelastic behavior, the solution we proposed in [12-14] was to replace Eq. (2) with its fractional counterpart:

$$\rho \frac{\mathrm{d}^n B(x,t)}{\mathrm{d}t^n} = H(x,t) - H_{stat}(B(x,t)) \tag{3}$$

where n is the fractional derivative order. Fractional differential equations are recommended for simulating viscoelasticity due to their ability to accurately capture memory-dependent behaviors and long-term responses exhibited by viscoelastic materials. Unlike classical derivatives, fractional derivatives account for past states, making them suitable for modeling dynamic hysteresis. They also handle heavy tail decays effectively and offer flexibility in adjusting models to match experimental data. Simultaneous resolution of Eq. (1) and Eq. (3) is possible through the concatenation in a unique expression. For this, Eq. (3) has to be reformulated in a way to isolate $\mathrm{d}B/\mathrm{d}t$:

$$\frac{\mathrm{d}^n B(x,t)}{\mathrm{d}t^n} = \frac{H(x,t) - H_{stat}(B(x,t))}{\rho} \tag{4}$$

$$\frac{\mathrm{d}B(x,t)}{\mathrm{d}t} = \frac{\mathrm{d}^{1-n}\left(\frac{H(x,t) - H_{\mathrm{stat}}(B(x,t))}{\rho}\right)}{\mathrm{d}t^{1-n}} \tag{5}$$

Once applied, the concatenation leads to Eq. (6)

$$\frac{1}{\sigma}\frac{\partial^2 H(x,t)}{\partial x^2} = \frac{\mathrm{d}^{1-n}\left(\frac{H(x,t) - H_{\mathrm{stat}}(B(x,t))}{\rho}\right)}{\mathrm{d}t^{1-n}} \tag{6}$$

Finite differences are used for the spatial term (left one) and Grünwald-Letnikov's definition for the fractional derivative term (right one) [15-17]. The resulting Eq. (7) - Eq. (9) are exclusively constituted of magnetic fields *H*-terms.

$$\frac{H(x-r,t) - 2H(x,t) + H(x+r,t)}{r^2} = \sigma \lim_{h \to 0^+} h^{n-1} \sum_{m=0}^{\infty} \frac{(n-1)_m}{m!} \frac{H(x,t-mh) - H_{\mathrm{stat}}(B(x,t-mh))}{\rho} \tag{7}$$

$$(n)_m = \frac{\Gamma(n+m)}{\Gamma(n)} = m \cdot (m+1) \cdot \mathrm{K} \cdot (m+n-1) \tag{8}$$

$$(m)_0 = 1 \tag{9}$$

where $(n)_m$ is the Pochhammer symbol and Γ the gamma function [18]. Applying Eq. (7) to every finite difference spatial discretization leads to a set of equations that can be converted into a matrix system, including a stiff matrix possibly set in pre-processing. The model input is H_{surf}, and the model outputs are the local evolution of $B(x,t)$ and $H(x,t)$. Since $H(x,t)$ and $B(x,t)$ are symmetric about the plane $x = \zeta / 2$, a resolution of Eq. (7) on the segment $[0, \zeta / 2]$ is enough, and a Neumann condition can be applied for the $x = \zeta / 2$ node. In this condition, r the space discretization in Eq. (7) is worth $\zeta / [2(N-1)]$, where N is the number of nodes. In the last stage, B_{a} is calculated by averaging the local induction (Eq. (10)):

$$B_{\mathrm{a}}(t) = \frac{\sum_{i=1}^{N} B(x_i,t)}{N} \tag{10}$$

B. 2nd Hysteresis Model: Extension of Bertotti's Loss Separation Theory to Include the Skin Effect

The second hysteresis model follows Bertotti's loss separation theory and directly separates the power losses into three contributions: the static hysteresis loss, the classical eddy current loss, and the excess loss [19, 20]. Correspondingly, the total magnetic field can also be separated into three contributions, as described in Eq. (11) [19],

$$H_{\mathrm{total}}(t,B) = H_{\mathrm{hy}}(B) + H_{\mathrm{cl}}(t,B) + H_{\mathrm{ex}}(t,B) \tag{11}$$

where H_{hy}, H_{cl}, and H_{ex} represent the static hysteresis field, the classical eddy current field, and the excess field.

We implemented the Preisach model, identified with sinusoidal waveforms of increasing amplitude for the static hysteresis field part. Eq. (12) detailed the static hysteresis field intensity H_{hy} calculated by the Preisach model.

$$H_{\mathrm{hy}}(B) = -E(B_0,b_0) + 2\sum_{i=1}^{m(t)} \left[E(B_i,b_{i-1}) - E(B_i,b_i)\right] \tag{12}$$

Where E is the inverse Everett function [21], B_i and b_i are the magnetic flux densities at the reversal points of the increasing and the decreasing branches, respectively, and $m(t)$ is a time-dependent variable representing the sampling steps. The Concentric Hysteresis Loops (CHLs) method [21, 22] was used to identify the inverse Everett function. An example of E is shown in Fig. 1.

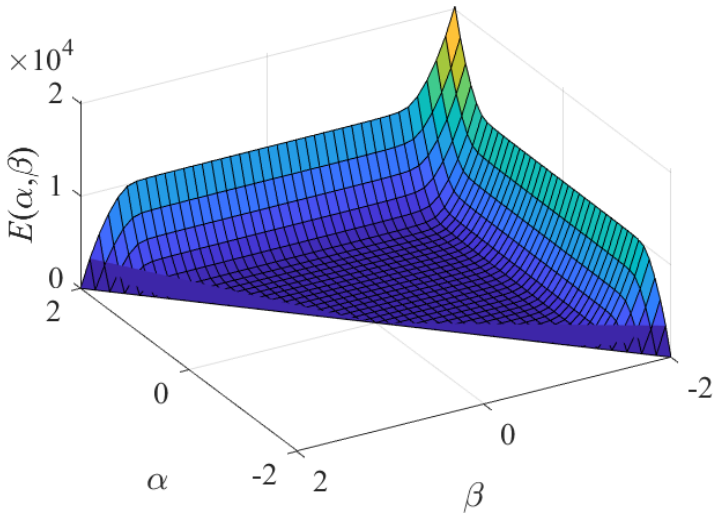

Fig. 1 – Inverse Everett function for the specimens tested in this study.

Then, we derived theoretical equations considering the skin effect based on Maxwell's equations for the classical eddy current contribution [23, 24]. Eq. (13) was solved through the so called linearization method of the magnetic permeability μ, using the experimental $B(H)$ curve.

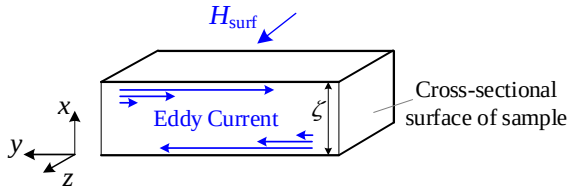

Fig. 2 – Cross-sectional surface of the silicon steel layer.

$$\begin{cases} \dfrac{\partial^2 H_k(x,t)}{\partial x^2} = \sigma\mu_k \dfrac{\partial H_k(x,t)}{\partial t} \\ B_k(x,t) = \mu_k H_k(x,t) \end{cases} \tag{13}$$

$H_k(x,t)$ is the local magnetic field in the z-direction; it is variational along the x-direction, considering the skin effect. The index k indicates the equations are satisfied at the time step where the k-th segment of the linearized $B(H)$ curve can represent the $B(H)$ relationship.

By imposing an average flux density B_a as described by Eq. (14), the local magnetic flux density $B(x,t)$ can be obtained by solving Eq. (15), where B_m is the average flux density peak value, ζ is the thickness of the steel sheet, j is the imaginary unit, ω is the angular frequency, and $\gamma_k = \zeta\sqrt{\omega\mu_k\sigma/2}$ is a parameter related to the skin depth.

Thus, the corresponding magnetic induction contribution of the classical eddy current field

$B_{cl,k}$ can be written as Eq. (16).

$$B_a(t) = B_m e^{-j\omega t} \tag{14}$$

$$B_k(x,t) = \frac{\cos\left(\gamma_k (1+j)\, x/\zeta\right)}{\cos\left(\gamma_k (1+j)/2\right)} B_m e^{-j\omega t} \tag{15}$$

$$B_{cl,k}(t) = B_a(t) - \frac{1}{\zeta}\int_{-\zeta/2}^{\zeta/2} B_k(x,t)\,dx \tag{16}$$

By substituting Eq. (16) into Eq. (13), the magnetic intensity on the surface and the local part of the steel sheet can be derived as Eq. (17) and Eq. (18), where F_k and φ_k are the coefficients related to the skin effect and indicated by Eq. (19). The derived classical eddy current field intensity is given in Eq. (20).

$$H_{surf,k}(t) = \frac{1}{\mu_k}\left\{B_m e^{-j\omega t}\right\} \tag{17}$$

$$H_k(t) = \frac{1}{\mu_k}\left\{F_k e^{-j\varphi_k} B_m e^{j\omega t}\right\} \tag{18}$$

$$\begin{cases} F_k = \dfrac{\sqrt{2}}{\gamma_k}\left[\dfrac{\cosh\gamma_k - \cos\gamma_k}{\cosh\gamma_k + \cos\gamma_k}\right]^{1/2} \\ \varphi_k = \operatorname{atan}\left(\dfrac{\sinh\gamma_k}{\sin\gamma_k}\right) - \dfrac{\pi}{4} \end{cases} \tag{19}$$

$$H_{cl}(t) = \mathrm{Re}\left[H_{surf}(t)\right] - \mathrm{Re}\left[H(t)\right] \tag{20}$$

To extend the applied excitation from sinusoidal waveforms into arbitrary non-sinusoidal waveforms of multi-harmonics, Eq. (21) and Eq. (22) are derived by Fourier decomposition.

$$B_{cl,arb}(t) = B_{m,1}\cos(\omega t) + \sum_{n=2}^{N} B_{m,n}\cos(n\omega t + \theta_n) \tag{21}$$

$$H_{cl,arb}(t) = \sum_{n=1}^{N} H_{cl,n}(t) \tag{22}$$

Thus, Eq. (22) can be implemented for predicting the classical eddy current field intensity under multi-harmonic conversions.

Finally, we implemented Eq. (23) for the excess field contribution [19]:

$$H_{ex}(t,B) = \sqrt{\sigma SGV_0}\,\delta\left|\frac{dB}{dt}\right|^{0.5} \tag{23}$$

where S is the electrical steel specimen cross-sectional area, G is a dimensionless constant setting as 0.1356 [19], V_0 is a statistic parameter depending on B's amplitude and frequency, and δ is sign(dB/dt) = ±1. Note that V_0 was identified using sinusoidal waveforms and kept unchanged for the simulation of non-sinusoidal ones. Experimental Results, Comparison Simulations/ Measurements

C. Experimental Setup.

An experimental setup was designed to measure the hysteresis cycles under various magnetic field configurations, including PWM-type working conditions. It operates under sinusoidal magnetic flux densities as required by international standards [25]. The excitation coil had 1033

turns, while the sensor coil had 120 turns. The tested specimen was a 50A470 ring-shaped sample with a 7700 kg·m^{-3} density. The specimen had an inner radius of 51 mm and an outer radius of 63.5 mm. This setup allowed for precise and reliable PWM-type measurements in close agreement with international standards.

D. Criteria of Hysteresis Model Evaluation.

When comparing ferromagnetic hysteresis models for predicting magnetic loss in a PWM converter, the most relevant criteria include accurately representing the dynamic hysteresis behavior under the PWM-specific working conditions (i.e., the ability to account for minor loop behavior). A model with fewer parameters is generally preferable for simplicity and ease of parameterization. Additionally, simulation time is critical, as faster models enable more efficient design iterations. The model's capability to return local information and detect local hot spots is also essential for identifying areas of potential thermal stress, which is critical for the reliability and longevity of the converter.

E. Results Under Different Levels of Magnetic Induction

The first set of results compares the simulation predictions with the experimental characterizations at various levels of B_m, while keeping the frequency fixed at f = 50 Hz. The comparison of dynamic hysteresis loops and associated losses is illustrated in Fig. 3 and summarized in Table I.

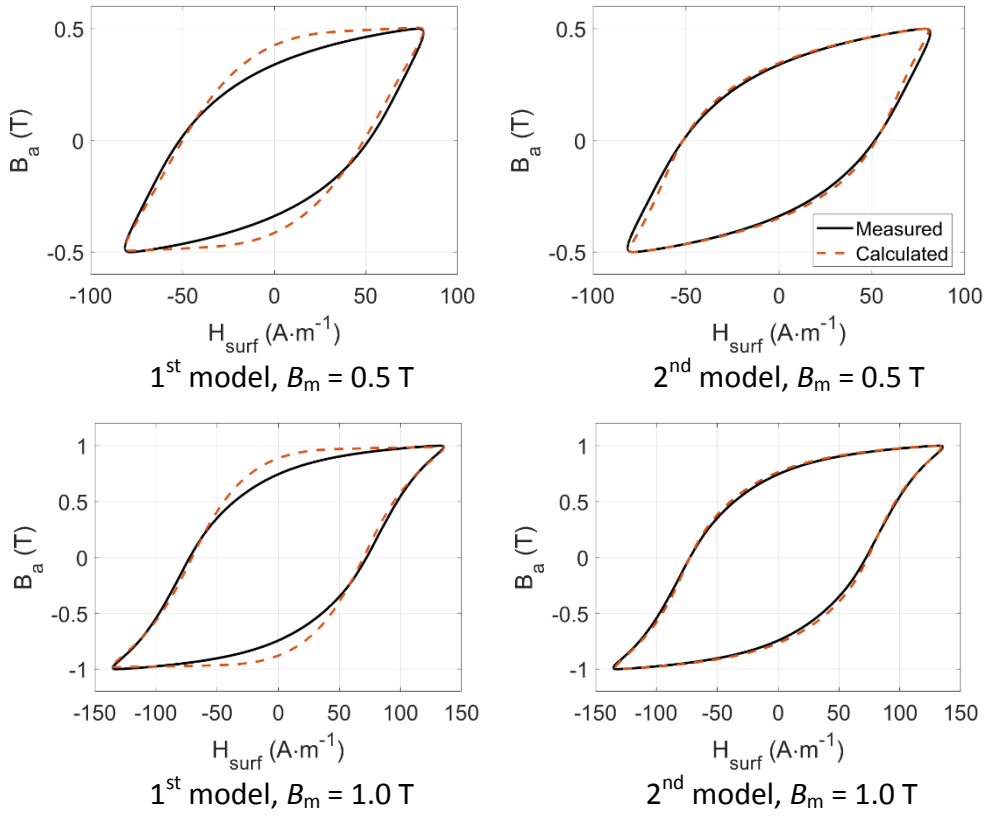

1st model, B_m = 0.5 T

2nd model, B_m = 0.5 T

1st model, B_m = 1.0 T

2nd model, B_m = 1.0 T

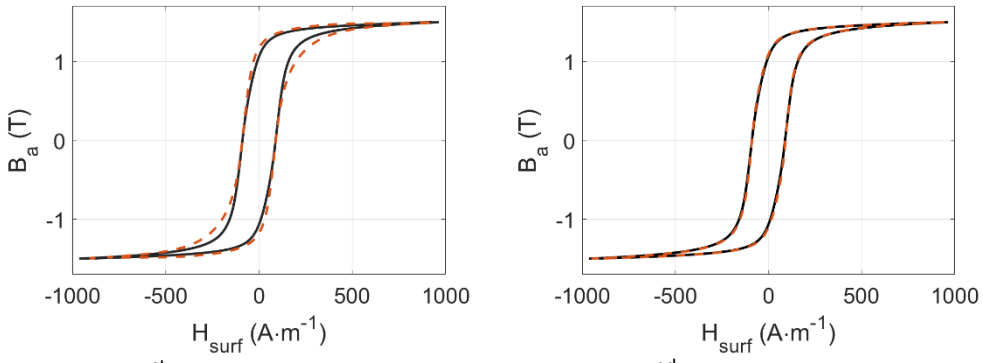

1st model, B_m = 1.5 T 2nd model, B_m = 1.5 T

Fig. 3 – Comparison simulation/measurement for the hysteresis cycle trajectory under sinusoidal B_a imposed conditions (f = 50 Hz).

Table. 1 – Loss comparison simulation/measurement for different magnetic flux density amplitudes.

Model	B_m/T	$W_{mea.}$/(W/kg)	$W_{cal.}$/(W/kg)				error/%
			static	classic	excess	total	
1st	0.5	0.515	0.303	0.266	0.006	0.575	11.6
	1.0	1.579	1.019	0.666	0.05	1.735	9.88
	1.5	3.416	2.52	1.012	0.102	3.634	6.38
2nd	0.5	0.515	0.418	0.085	0.009	0.513	0.40
	1.0	1.579	1.206	0.342	0.062	1.61	1.93
	1.5	3.416	2.596	0.768	0.081	3.446	0.86

Note: Sinusoidal excitation with 50 Hz is applied in the table.

F. Results Under Different Levels of Frequencies.

The second set of results compares the simulation predictions with the experimental characterizations at various frequency levels, while keeping B_m constant. The comparison of the dynamic hysteresis loops and associated losses is illustrated in Fig. 4 and summarized in Table II.

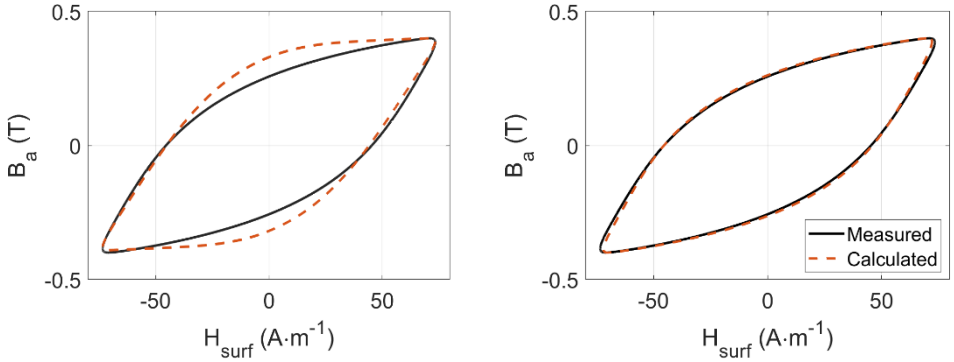

1st model, f = 50 Hz 2nd model, f = 50 Hz

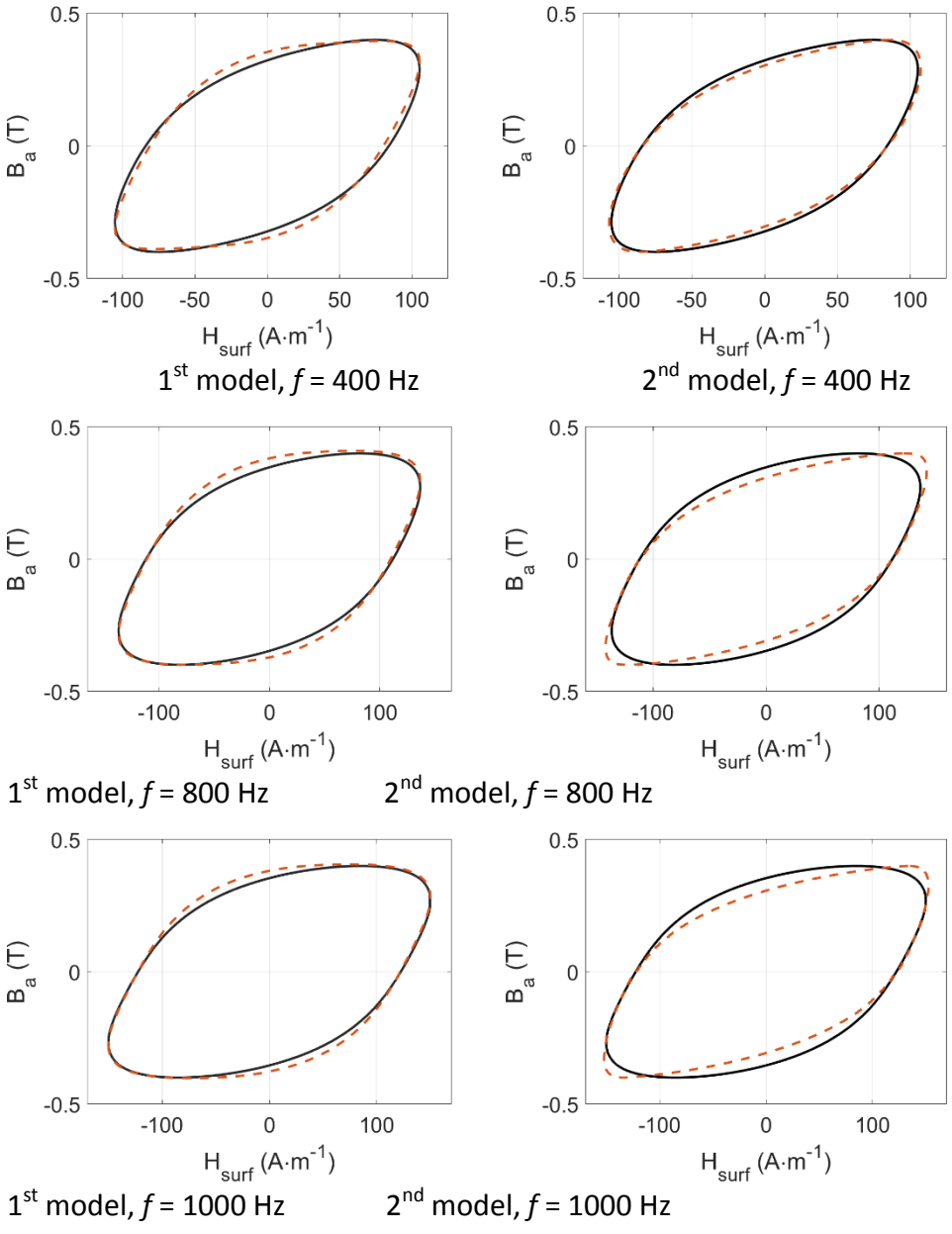

1st model, f = 400 Hz 2nd model, f = 400 Hz

1st model, f = 800 Hz 2nd model, f = 800 Hz

1st model, f = 1000 Hz 2nd model, f = 1000 Hz

Fig. 4 – Comparison simulation/measurement for the hysteresis cycle trajectory during a sinusoidal conversion (B_m = 0.4 T).

Table. 2 – Loss comparison simulation/measurement for different frequencies.

Model	f/Hz	$W_{mea.}$/(W/kg)	$W_{cal.}$/(W/kg)				error/%
			static	classic	excess	total	
1st	50	0.355	0.215	0.188	0.005	0.407	14.65
	400	5.61	2.011	3.352	0.378	5.741	2.34
	800	15.43	4.685	9.858	1.763	16.3	5.64
	1000	21.47	6.08	13.766	2.818	22.66	5.54
2nd	50	0.355	0.294	0.054	0.008	0.358	0.57
	400	5.61	2.356	3.055	0.03	5.441	3.01
	800	15.43	4.712	7.712	2.172	14.6	5.43
	1000	21.47	5.89	9.632	4.252	19.77	7.91

Note: Sinusoidal excitation with 0.4 T is applied in the table.

G. Results Under PWM-Type Conversion.

Fig. 5 below compares the simulation results obtained with the 1st and the 2nd model to the experimental results obtained in PWM-type conditions (B_m = 1.1 T, f = 50 Hz fundamental combined with B_m = 0.1 T, f = 1 kHz harmonic 20).

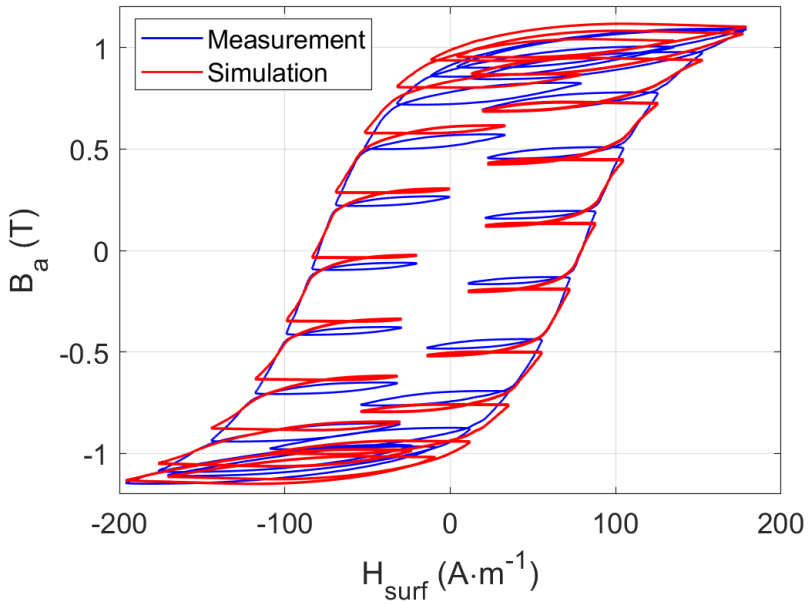

1st model – PWM

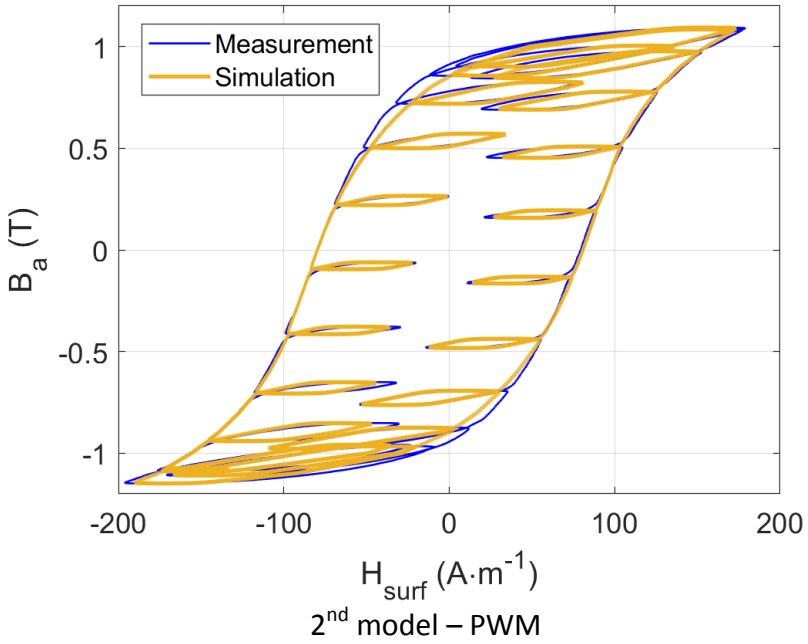

Fig. 5 – Comparison simulation/measurement for the hysteresis cycle trajectory in PWM-type conditions.

Table. 3 – Loss comparison simulation/measurement during PWM-type conversion.

Model	$W_{mea.}$/(W/kg)	$W_{cal.}$/(W/kg)				error/%
		static	classic	excess	total	
1st	2.721	0.795	1.617	0.06	2.472	9.15
2nd	2.721	1.476	1.035	0.053	2.565	5.74

Note: PWM-type excitation with fundamental wave parameters of 1.1 T and 50 Hz is applied in the table.

H. Discussion.

Both models described in this manuscript require a static hysteresis component for proper operation, denoted as H_{stat} for the 1st model and H_{hy} for the 2nd. Although not explicitly mentioned in the descriptive section, the Jiles-Atherton model in its inverse configuration [10] was used for all comparisons and simulations/measurements of the 1st model. Nevertheless, the Preisach model, which was applied to the 2nd model, could have been equally effective. Consequently, when comparing simulation methods, it is more appropriate to focus on the dynamic aspects. Table IV below outlines the dynamical simulation parameters and specifies the experimental data necessary for their calibration.

Table. 4 – Identified parameters/measures results required for the prediction during PWM-type conversion.

	List of Dynamical parameters	List of required experimental data
1st Model	ρ, n	*_ a low-frequency major hysteresis cycle (Bm = 1.1 T, f = 50 Hz)* *_ a high-frequency major hysteresis cycle (Bm = 1.1 T, f = 1 kHz)*
2nd Model	μ_k, V_0	*_ a low-frequency major hysteresis cycle (Bm = 1.1 T, f = 50 Hz)* *- initial B-H curve*

Table 5 summarizes the comparison of both models based on the most relevant criteria outlined below:

_ Accuracy: Ability to accurately predict hysteresis loops, including their shape, area, and other key features.

_ Applicability: Dependence on frequency and material specificity.

_ Computational efficiency: Simulation time and computational complexity.

_ Stability: Numerical stability and consistency of simulation results.

_ Parameterization: Number of parameters required.

_ Implementation: Effort required to configure the model parameters.

_ Predictive capability: Capacity to predict behaviors beyond the scope of experimental observations.

Table. 5 – Most relevant criteria of the tested models for the prediction during PWM-type conversion.

Model	1st Model	2nd Model
Accuracy	< 10 % whatever the frequency range	< 5 %, in the low-frequency range
Applicability	Easy to switch from one material to another	Easy to switch from one material to another
Computational efficiency	< 1min / hysteresis loop	3.96 s / hysteresis loop
Parameterization	2 dynamical parameters	2 dynamical parameters
Implementation	Moderately easy to implement	Easy to implement
Predictive capability	Accurate, up to 10 kHz [12]	Limited in the high-frequency range

It is important to note that certain criteria hold greater relevance than others, depending on the specific context of the PWM-type application examined in this work. For example,

computational efficiency becomes a critical factor when a large number of hysteresis models must be executed simultaneously, such as in the space-discretized resolution of electromagnetic problems. However, this criterion is less significant when the focus shifts to predicting magnetic losses and their frequency dependence like in the PWM-type context.

Both simulation methods exhibit similar characteristics in terms of applicability and parameterization. The second model demonstrates greater accuracy in the low-frequency range, with significantly faster simulation times and easier implementation. In contrast, the first model excels in the high-frequency range and offers superior predictive capability. Although not explicitly indicated in Table IV, the first model provides additional insights, such as the distribution of magnetic losses across the thickness of the tested specimen (as illustrated in Fig. 6).

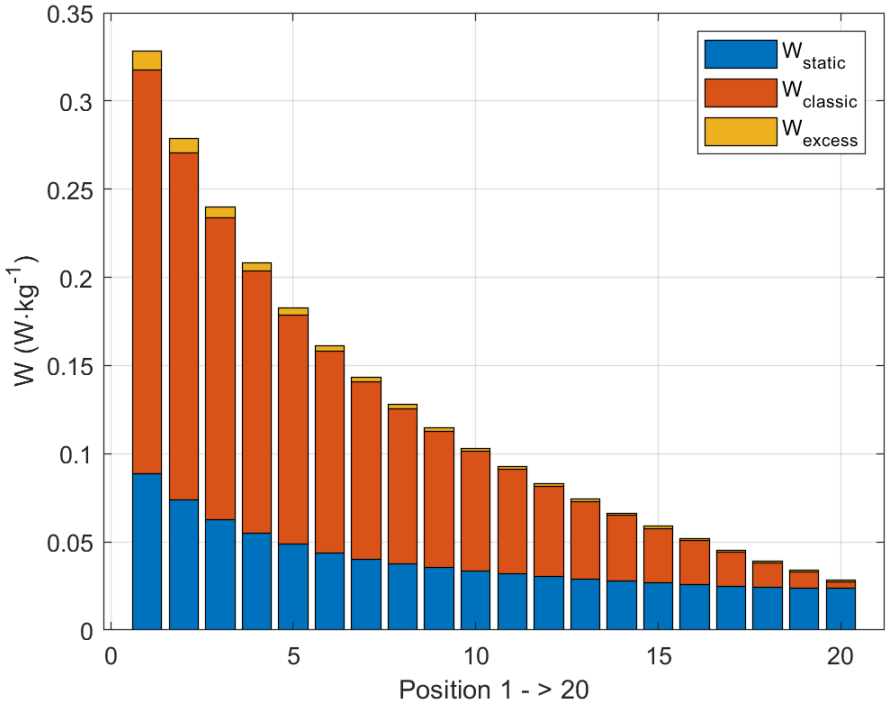

Fig. 6 – Simulated loss at different positions of the specimen cross-section with the 1st model.

III - Conclusion

This study provided a comprehensive comparison between two hysteresis models applied to the simulation of magnetic losses in electrical steel components under PWM-type conversion. The models were rigorously evaluated against key criteria such as accuracy, computational efficiency, stability, parameterization, and predictive capability. Both models demonstrated distinct strengths depending on the frequency range and the specific simulation context. The second model, while simpler to implement and more computationally efficient, proved highly effective in simulating low-frequency magnetic behavior with greater accuracy and faster simulation times. Conversely, the first model exhibited superior performance in high-frequency

simulations and offered enhanced predictive capabilities. It can also provide the spatial distribution of magnetic losses which can be useful during design optimization.

Our analysis highlighted the importance of selecting the appropriate simulation method based on the intended application. For scenarios requiring the simultaneous execution of numerous hysteresis models, such as in the space-discretized resolution of electromagnetic problems, computational efficiency becomes dominant. However, when focusing on magnetic loss predictions and their frequency dependencies, the first model's predictive capabilities may offer valuable additional insights that justify its increased computational complexity. Overall, the findings of this study underscore the need for a balanced consideration of accuracy, computational demand, and application-specific requirements when choosing between hysteresis models. The insights derived from this comparative analysis offer practical guidance for optimizing magnetic component simulations within PWM-type converters, enhancing the design and performance of future power conversion systems.

References

[1] M.S. Rylko, K.J. Hartnett, J.G. Hayes, and M.G. Egan, M.G., "Magnetic material selection for high power high frequency inductors in dc-dc converters," in *2009 Twenty-Fourth Annual IEEE Applied Power Electronics Conference and Exposition,* pp. 2043-2049, IEEE, 2009.

[2] P. Rasilo, W. Martinez, K. Fujisaki, J. Kyyrä, and A. Ruderman, "Simulink model for PWM-supplied laminated magnetic cores including hysteresis, eddy-current, and excess losses," *IEEE Transactions on Power Electronics*, vol. 34, no. 2, pp. 1683-1695, 2018.

[3] B.J. Lyons, J.G. Hayes, and M.G. Egan, "Magnetic material comparisons for high-current inductors in low-medium frequency dc-dc converters," in *APEC 07-Twenty-Second Annual IEEE Applied Power Electronics Conference and Exposition* (pp. 71-77). IEEE, 2007.

[4] A.J. Moses, "Electrical steels: past, present and future developments," *IEE Proceedings A (Physical Science, Measurement and Instrumentation, Management and Education)*, *137*(5), pp.233-245, 1990.

[5] D. Ruiz-Robles, J. Ortíz-Marín, V. Venegas-Rebollar, E.L. Moreno-Goytia, D. Granados-Lieberman, J.R. Rodríguez-Rodriguez, "Nanocrystalline and silicon steel medium-frequency transformers applied to DC-DC converters: analysis and experimental comparison," *Energies*, *12*(11), p.2062, 2019.

[6] P. Nakmahachalasint, K.D. Ngo, and L. Vu-Quoc, A static hysteresis model for power ferrites. *IEEE transactions on power electronics*, *17*(4), pp.453-460, 2002.

[7] M.A. Raulet, B. Ducharne, J.P. Masson, and G. Bayada, "The magnetic field diffusion equation including dynamic hysteresis: a linear formulation of the problem," IEEE transactions on magnetics, 40(2), pp.872-875, 2004.

[8] E. D. Torre, Magnetic hystereis, IEEE Press, New York, 1999

[9] D. C. Jiles, and D. L. Atherton, "Theory of ferromagnetic hysteresis," J. Magn. Magn. Mater., vol. 61, nos. 1–2, pp. 48–60, 1986.

[10] P. Fagan, B. Ducharne, and A. Skarlatos, "Optimized magnetic hysteresis management in numerical electromagnetic field simulations," In *2021 IEEE International Magnetic Conference (INTERMAG)* (pp. 1-5). IEEE, 2021.

[11] R.M. Bozorth, Ferromagnetism (p. 992), 1993.

[12] B. Ducharne, H. Hamzehbahmani, T. Gao, P. Fagan, and G. Sebald, "High-frequency fractional predictions and spatial distribution of the magnetic loss in a grain-oriented magnetic steel lamination," Fractal and Fractional, 8(3), p.176, 2024.

[13] B. Ducharne, H. Hamzehbahmani, R.V. Sabariego, and Y. Gao, "Magnetic behavior of a laminated magnetic core in the presence of interlaminar faults: A simulation method based on fractional operators," Journal of Magnetism and Magnetic Materials, p.172278, 2024.

[14] B. Ducharne, and G. Sebald, "Combining a fractional diffusion equation and a fractional viscosity-based magneto dynamic model to simulate the ferromagnetic hysteresis losses," AIP Advances, 12(3), 2022.

[15] K. Oldham, and J. Spanier, "The fractional calculus theory and applications of differentiation and integration to arbitrary order," Elsevier, 1974.

[16] B. Ducharne, and G. Sebald, "Fractional derivatives for the core losses prediction: State of the art and beyond," Journal of Magnetism and Magnetic Materials, 563, p.169961, 2022.

[17] D. Valério, J.J. Trujillo, M. Rivero, J.P. Machado, and D. Baleanu, "Fractional calculus: A survey of useful formulas," The European Physical Journal Special Topics, 222(8), pp.1827-1846, 2013.

[18] R. Şahin, and O. Yağcı, "A new generalization of pochhammer symbol and its applications," Applied Mathematics and Nonlinear Sciences, 5(1), pp.255-266, 2020.

[19] G. Bertotti, "*Hysteresis in magnetism: for physicists, materials scientists, and engineers*," Gulf Professional Publishing, 1998.

[20]G. Bertotti, “A general statistical approach to the problem of eddy current losses,” *Journal of magnetism and Magnetic Materials*, *41*(1-3), pp.253-260, 1984.
[21]Z. Szabó, and J. Füzi, “Implementation and identification of Preisach type hysteresis models with Everett Function in closed form,” *Journal of Magnetism and Magnetic Materials*, *406*, pp.251-258, 2016.
[22]X. Zhao, X. Wu, H. Wang, and Y. Miao, “A dynamic hysteresis prediction model of grain-oriented silicon steel sheet under AC-DC hybrid magnetization,” *Journal of Magnetism and Magnetic Materials*, vol. 587, 2023, art. no. 171269.
[23]H. Wang, X. Zhang, X. Zhao, X. Wu, and Y. Miao, “A dynamic hysteresis model for ultra-thin GO silicon steel under multi-harmonic excitation,” *2023 IEEE International Conference on Applied Superconductivity and Electromagnetic Devices (ASEMD)*, Tianjin, China, 2023.
[24]S. Gao, X. Zhao, and L. Liu, “Dynamic hysteresis and loss prediction of GO silicon steel under high-frequency excitation with DC-bias,” *2023 IEEE International Conference on Applied Superconductivity and Electromagnetic Devices (ASEMD)*, Tianjin, China, 2023.
[25]IEC 60404-6, “Magnetic materials – Part 6: Methods of measurement of the magnetic properties of magnetically soft metallic and powder materials at frequencies in the range 20 Hz to 100 kHz by the use of ring specimens,” International Electrotechnical Commission, 2010.